物 理 化 学 学 报
Acta Phys. -Chim. Sin. **2019,** *35* (5), 523–530

[Article] doi: 10.3866/PKU.WHXB201806191 www.whxb.pku.edu.cn

Molybdenum Carbide Prepared by a Salt Sealing Approach as an Electrocatalyst for Enhanced Hydrogen Evolution Reaction

LIN Zhou, SHEN Linfan, QU Ximing, ZHANG Junming, JIANG Yanxia *, SUN Shigang
State Key Laboratory of Physical Chemistry of Solid Surfaces, Department of Chemistry, College of Chemistry and Chemical Engineering, Xiamen University, Xiamen 361005, Fujian Province, P. R. China.

Abstract: Molybdenum carbide is regarded as an excellent substitute for Pt-based catalysts in the hydrogen evolution reaction (HER), owing to its low cost, superior catalytic performance, and long-term stability. In this work, salt-sealed molybdenum carbide was prepared using sodium molybdate and 2,6-diaminopyridine as the reactive raw materials, followed by continuous salt sealing and calcination of the precursor under an inert atmosphere. The morphology, composition and structure of salt-sealed molybdenum carbide were determined by scanning electron microscopy, transmission electron microscopy (TEM), energy-dispersive X-ray spectroscopy (EDS), X-ray diffraction (XRD), and X-ray photoelectron spectroscopy (XPS). The results indicate that salt-sealed molybdenum carbide has irregular morphology and includes nanoparticles and nanorods. A comparison of the TEM images of Mo_2C with salt sealing (Mo_2C/SS) and Mo_2C without salt sealing (Mo_2C) indicates that Mo_2C/SS exhibits a smaller particle size. This suggests that salt sealing can efficiently avoid particle aggregation. The Brunauer-Emmett-Teller (BET) specific surface area of the catalysts was obtained from nitrogen adsorption/desorption isotherms. The increase in BET surface area from 2.55 to 8.14 $m^2 \cdot g^{-1}$ after salt sealing provides evidence for the formation of pores in the product. The results of XRD, EDS and XPS analyses show that Mo_2C/SS has an orthorhombic crystal structure with molybdenum oxides on the surface, which may originate from surface oxidation. Considering the results of XPS and the turnover frequency (TOF) calculation, we can conclude that the formation of pores *via* salt sealing contributes to the exposure of more active sites, while simultaneously enlarging the contact area with oxygen. Therefore, higher molybdenum oxide content is generated on the surface, resulting in a lower proportion of active centers (molybdenum carbides) on the catalyst surface. Furthermore, the pseudocapacitance generated by the faradaic reaction of molybdenum oxides is superimposed on the double-layer capacitance of Mo_2C catalysts, which increases the double layer capacitance. Since the effect of pseudo-capacitance on Mo_2C/SS is more significant, the TOF number declines after salt sealing. Compared with Mo_2C, Mo_2C/SS exhibits three features that promote HER mass activity: (1) the generation of large quantities of pores *via* salt sealing leads to an increase in the BET surface area and exposure of more active sites, which is beneficial for improving HER performance; (2) the porous structure and enlarged surface area pave the way for effective mass and charge transfer; (3) the decrease of the Tafel slope from 145 to 88 $mV \cdot dec^{-1}$. In summary, salt-sealed Mo_2C exhibited enhanced HER activity with an overpotential of 175 mV to achieve a current density of 10 $mA \cdot cm^{-2}$. The Tafel slope for HER on salt-sealed Mo_2C is 88 $mV \cdot dec^{-1}$. This can be considered as the proof of the Volmer-Heyrovsky mechanism with electrochemical desorption as the rate-determining step.

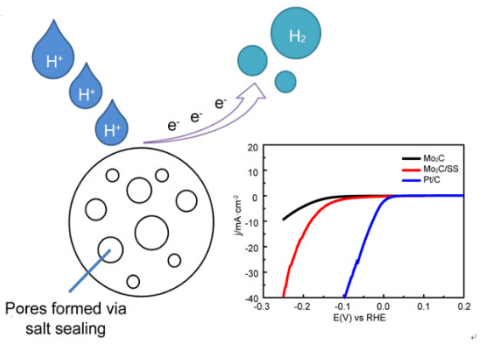

Key Words: Molybdenum carbide; Hydrogen evolution reaction; Salt sealing; Active site; Electrocatalysis

Received: April 11, 2018; Revised: June 12, 2018; Accepted: June 12, 2018; Published online: June 19, 2018.
*Corresponding author. Email: yxjiang@xmu.edu.cn.
The project was supported by the National Key Research and Development Program of China (2017YFA0206500) and the National Natural Science Foundation of China (21773198, U1705253).
国家重点研究与发展项目(2017YFA0206500)和国家自然科学基金(21773198, U1705253)资助

盐封后碳化钼电催化剂的制备及其氢析出性能

林舟，申琳璠，瞿希铭，张俊明，姜艳霞*，孙世刚
厦门大学化学与化工学院化学系，固体表面物理化学国家重点实验室，福建 厦门 361005

摘要：碳化钼具有低廉的价格、优越的催化性能以及良好的稳定性而被人们认为是极好的可以替代Pt等贵金属的氢析出反应(HER)催化剂。本工作采用钼酸钠和2,6-二氨基吡啶为反应原料，之后不断进行盐封的过程直到前驱体被紧紧包覆在NaCl的晶格中，最后置于惰性气氛下煅烧即可制得盐封后碳化钼。本工作采用了扫描电子显微镜(SEM)、透射电子显微镜(TEM)、能量色散x射线光谱(EDS)、X射线衍射(XRD)以及X射线光电子能谱(XPS)等技术对盐封后碳化钼的形貌、组成以及晶体结构进行了表征。结果表明盐封后的产物形貌并不均一，其中包括纳米颗粒及纳米棒。比较Mo_2C/SS与Mo_2C的TEM图，可以发现盐封后Mo_2C的尺寸变小，表明盐封的方法可以有效地避免颗粒的团聚。根据产物的氮气吸脱附等温线得到的催化剂的Brunauer-Emmett-Teller (BET)比表面积，盐封后Mo_2C的BET表面积由2.55提高至8.14 $m^2 \cdot g^{-1}$，可以证明盐封过程中孔的生成。EDS、XRD及XPS分析的结果表明盐封后的产物是斜方晶系的Mo_2C，并且表面由于被氧气氧化而带有氧化钼。结合XPS和周转率(TOF)数计算的结果，可以说明盐封过程中孔的形成有助于暴露更多活性位点，然而同时也扩大了与氧气的接触面积，催化剂表面形成的氧化钼的含量也增多。因此，催化剂表面活性中心即碳化钼所占的比例降低。另一方面，氧化钼的法拉第反应产生的赝电容会与碳化钼催化剂的双电层电容叠加，导致得到的比容量数值偏大。而氧化钼的赝电容效应对Mo_2C/SS催化剂的影响是更显著的，因此盐封后的TOF数降低。同Mo_2C相比，Mo_2C/SS展现出更高的HER质量活性的原因可归结如下：(1)盐封过程中大量孔的形成有助于提高产物的BET表面积并暴露出更多的活性位点；(2)盐封后的多孔结构和较大的表面积有利于传质传荷；(3)盐封后碳化钼的Tafel斜率由145降至88 $mV \cdot dec^{-1}$。总的来说，盐封后碳化钼的HER活性有了明显的提高，当电流密度达到10 $mA \cdot cm^{-2}$时，过电位为175 mV左右。盐封后碳化钼的Tafel斜率为88 $mV \cdot dec^{-1}$，证明催化剂表面发生的氢析出反应遵循Volmer-Heyrovsky机理并以电化学脱附步骤为反应的速控步骤。

关键词：碳化钼；氢析出反应；盐封；活性位点；电催化
中图分类号：O646

1 Introduction

Hydrogen, as a clean and renewable energy source, has drawn increasing attention for its promising alternative to traditional carbonaceous fuel [1]. In recent years, water splitting is one of the most attractive methods for sustainable hydrogen production [2–5]. As for the hydrogen evolution reaction (HER), noble metal Pt-based catalysts have exhibited superior catalytic activity with low overpotential and high energy conversion efficiency, while both the high cost and rare storage limit their large-scale applications. Therefore, it is essential to explore inexpensive, highly active and earth-abundant catalysts for HER [6,7].

Currently, various combinations of metals (Pt, Pd, Ir, Ru, Ni), metal alloys (PtNi, PtPd, NiCo, NiMo, NiMn), substrates with 3*d* transition metal hydroxides ($Ni(OH)_2$, $Co(OH)_2$, $Fe(OH)_2$, $Mn(OH)_2$), 3*d* transition metal phosphides (CoP, NiP, FeP, Cu_3P), 3*d* transition metal carbides (WC_x, MoC_x) and transition metal sulfides (MoS_2, CoS_2, FeS_2, Mo_3S_{13}, NiS_2) are used to catalyze the conversion of H_3O^+ (acid) or H_2O (alkaline) to H_2 [8–12].

Transition metal carbides have been known as the most promising substitutes for Pt-based catalysts in consideration of their similar *d*-band electronic structures and catalytic properties to platinum group metals [13,14]. Among them, molybdenum carbide has been identified as an excellent HER electrocatalyst because of its low price, outstanding electrical conductivity, high chemical durability and catalytic activity [15,16]. For instance, Cui *et al*. [17] prepared Mo_2C nanoparticles loaded on graphitic carbon sheets (Mo_2C/GCSs) and found that the existence of carbon support can inhibit the aggregation of the product, resulting in more exposed active sites. Therefore, the synthesized Mo_2C/GCSs exhibited high catalytic efficiency with excellent chemical stability and small charge transfer resistance. Liao *et al*. [18] developed a nanoporous Mo_2C nanowire composed of Mo_2C nanocrystallites, the enriched nanoporosity and large reactive surface contribute to their superior HER activity with a Tafel slope of only 53 $mV \cdot dec^{-1}$.

Ding *et al*. [19] adopted the approach of salt sealing to achieve high efficiency of morphology controlling and the obtained porous structure, which paved the way for acting as an outstanding catalyst for oxygen reduction reaction. Salt sealing was carried out by the loop repetition the process that the addition of oversaturated NaCl solution, water evaporation and NaCl recrystallization until the precursor was completely covered and buried by the recrystallized NaCl crystal. The precursor was tightly sealed by salt through salt sealing and its

original three-dimensional morphology would be fixed in the crystal. Therefore, the original morphology of the product would be well preserved in the subsequent annealing process. In addition, the precursor was tightly sealed inside the lattice of NaCl *via* salt sealing and so in the process of annealing the NaCl crystal served as a fully sealed container. The annealing in such a closed reactor would generate large quantities of pores in the product, which was beneficial to increasing the BET specific surface area. Increasing the surface area would expose more active sites and improve the HER performance.

In this work, the salt sealing approach was adopted to create pores in prepared Mo_2C, aiming at obtaining enriched nanoporosity with more exposed active sites and larger surface area.

2 Experimental

2.1 Reagents

All of the reagents were used as received without further purification. Sodium molybdate (AR), sodium chloride (AR), ethanol (AR), isopropanol (AR), concentrated hydrochloric acid (AR) were purchased from Sinopharm Chemical Reagent limited corporation. 2,6-diaminopyridine (99%) was obtained from J&K Chemicals.

2.2 Synthesis of Mo_2C

0.01 mol Na_2MoO_4 and 0.02 mol 2,6-diaminopyridine (DAP) were dissolved in 200 mL distilled water, then diluted hydrochloric acid (pH = 1) was added dropwise with magnetic stirring at room temperature until a white precipitate was obtained at pH = 5–6. Then adjust the pH of the solution to 4 and no more precipitate was generated with the subsequent addition of HCl. After stirring the solution at 50 °C for 5 h，the white precipitate turned into yellow, which means the formation of DAP-$2H^+/MoO_4^{2-}$. Then the yellow precipitate was filtered and washed with distilled water for three times. After that, part of the precursor DAP-$2H^+/MoO_4^{2-}$ was directly annealed at 900 °C for 3 h in the atmosphere of argon, followed by acid treatment, centrifugation and drying process to gain the Mo_2C without salt sealing (Mo_2C). The other part of the obtained yellow precipitate was dispersed in 15 mL of oversaturated NaCl solution and magnetic stirring was sustained for 2 h to get the homogeneous dispersion. After that, heat the dispersion in a water bath of 60 °C to evaporate off containing water; at the same time the oversaturated NaCl solution at 80 °C was continually and slowly added into the dispersion, until the precursor DAP-$2H^+/MoO_4^{2-}$ was covered and buried by the recrystallized NaCl. After the process of salt sealing, place the precursor inside the vacuum dryer at 60 °C for 24 h and then anneal at the temperature of 900 °C for 3 h under flowing argon. Finally, the appropriate amount of hot hydrochloric acid was added to remove the NaCl crystal. After acid treatment, the Mo_2C with salt sealing (Mo_2C/SS) will be obtained.

2.3 Physical characterization

SEM and TEM images were obtained respectively on Japanese Hitachi S-4800 and JEM-1400 with the accelerated voltage of 100 kV, which is produced by Japanese JEOL. HRTEM patterns were taken on TECNAI-F30 with the accelerated voltage of 300 KV, which is produced by Holland Philip-FEI. XRD characterization was collected on Bruker D8 Advance X-ray diffractometer (Cu K_α, 40 kV, 40 mA) produced by Bruker company in Germany. XPS measurements were acquired from Quantum 2000 X-ray photoelectron spectrometer produced by Physical electronics company in the United States.

2.4 Electrochemical measurements

4 mg Mo_2C were dispersed in 1 mL of solution consisted of 1 : 1 (*V*/*V*) distilled water and ethanol containing 10 μL Nafion (5%, mass fraction) and the homogeneous ink would be obtained by ultrasonic treatment. Then 10 μL of the ink was loaded on the surface of the glassy carbon electrode (5 mm in diameter) with a catalyst loading of 0.204 $mg \cdot cm^{-2}$. During the process of electrochemical performance testing, the CHI660E electrochemical workstation was used as the testing instrument and the standard three-electrode system was adopted with a modified glassy carbon electrode as the working electrode, a saturated calomel electrode as the reference electrode and graphite carbon as the auxiliary electrode. All electrochemical measurements were performed in a deaerated 0.1 $mol \cdot L^{-1}$ $HClO_4$ solution. The HER polarization curves of catalysts were obtained by linear sweep voltammetry (LSV) at a scan rate of 5 $mV \cdot s^{-1}$ at a constant temperature of 30 °C in a water bath.

3 Results and discussion

The SEM image in Fig. 1a reveals the irregular morphology of Mo_2C/SS, including nanoparticles and nanorods. The SEM image of the precursor DAP-$2H^+/MoO_4^{2-}$ was placed in Supporting Information Fig. S1, the irregular morphology is consistent with Mo_2C/SS, which proves that the original morphology of the product can be well preserved by salt sealing. The EDS pattern of the product in Fig. 1b reflects the existence of C, O, Mo elements. Fig. 1c exhibits the XRD characterization of Mo_2C/SS, which confirms that the product belongs to orthorhombic crystal system. The HRTEM image in Fig. 1d shows the obvious lattice fringes with a distance of 0.228 nm, which corresponds to the (102) crystal plane of orthorhombic Mo_2C. The HRTEM result is consistent with XRD characterization.

Fig. 2a, b are the TEM images of Mo_2C with and without salt sealing respectively, we can see that the size of Mo_2C/SS is smaller in comparison, indicating that salt sealing can efficiently avoid particle aggregation. The nitrogen adsorption/desorption isotherms of Mo_2C in Fig. 2c, d show that the BET specific surface area rises from 2.55 to 8.14 $m^2 \cdot g^{-1}$ *via* salt sealing and prove the generation of pores in the product.

As shown in Fig. 3a, b, the Mo 3*d* XPS spectra of Mo_2C

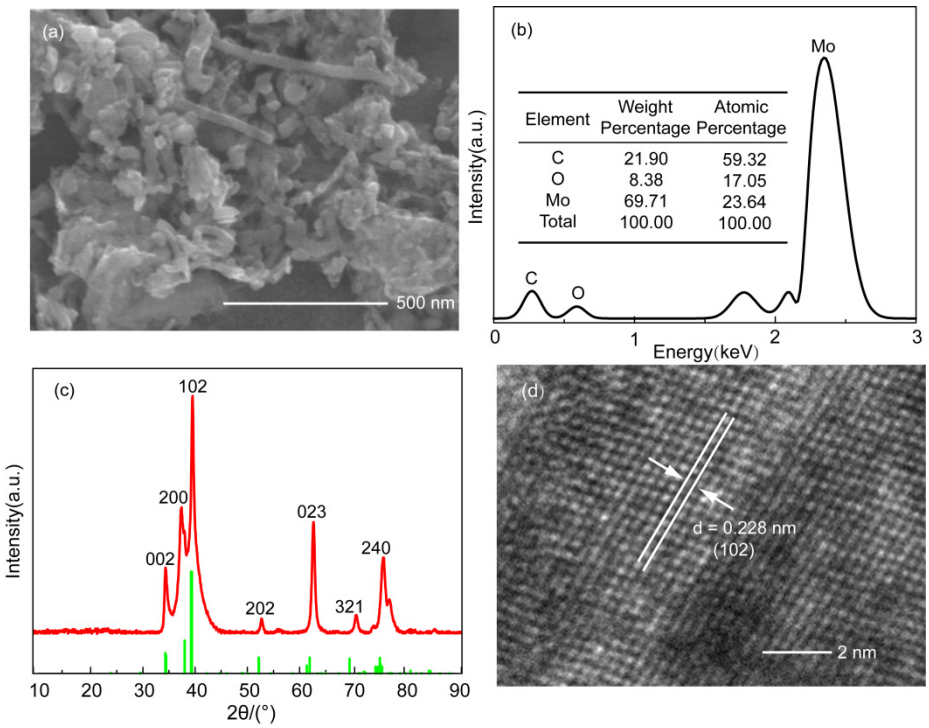

Fig. 1 (a) SEM image; (b) EDS pattern; (c) XRD pattern (the inset shows the pattern of orthorhombic Mo_2C in standard card) and (d) HRTEM image of Mo_2C/SS.

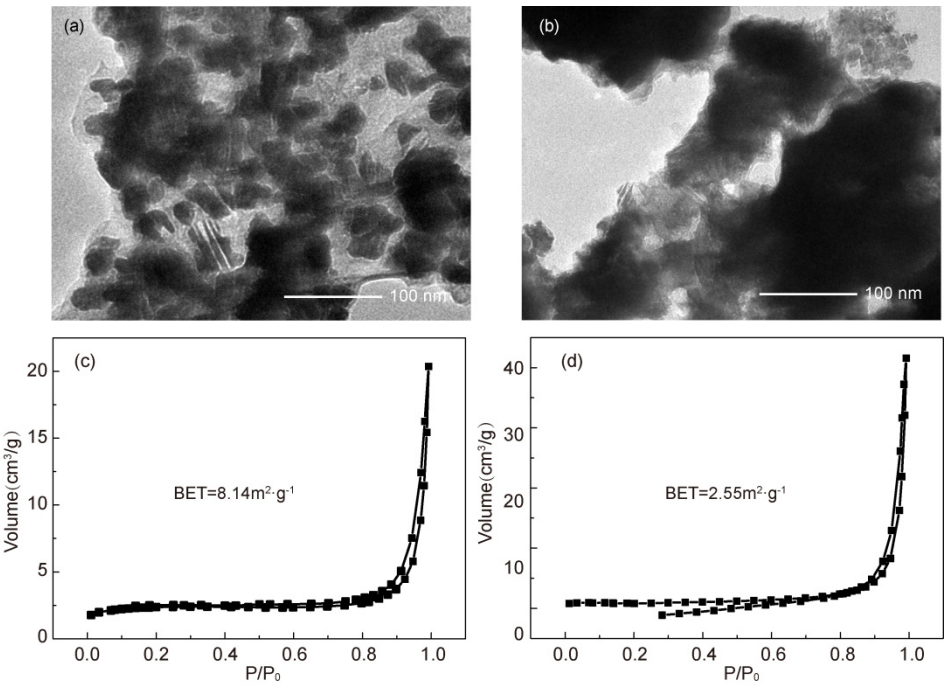

Fig. 2 TEM images of Mo_2C/SS (a) and Mo_2C (b); Nitrogen adsorption/desorption isotherms of Mo_2C/SS (c) and Mo_2C (d).

were deconvoluted into six peaks, corresponding to Mo^{2+}, Mo^{4+} and Mo^{6+} species. As reported in previous articles, Mo^{2+} is assigned to molybdenum carbides and serves as active sites for HER [20]. Mo^{4+} and Mo^{6+} can be assigned to molybdenum oxides (MoO_2 and MoO_3) possibly from the surface oxidation of Mo species, as observed in previous reports [21]. The surface MoO_2 and MoO_3 can be removed after activation [22]. Table 1 displays the peak position and percentage of Mo at different valence state in Mo_2C, it can be seen that the percentage of molybdenum oxides in the product increases after salt sealing, which can be attributed to the generation of a large number of pores during the process of salt sealing. The generation of pores will enlarge the contact area with oxygen, which leads to the higher percentage of molybdenum oxides on the surface.

Fig. 4a displays the polarization curves of catalysts, the commercial Pt/C is measured for comparison with the highest

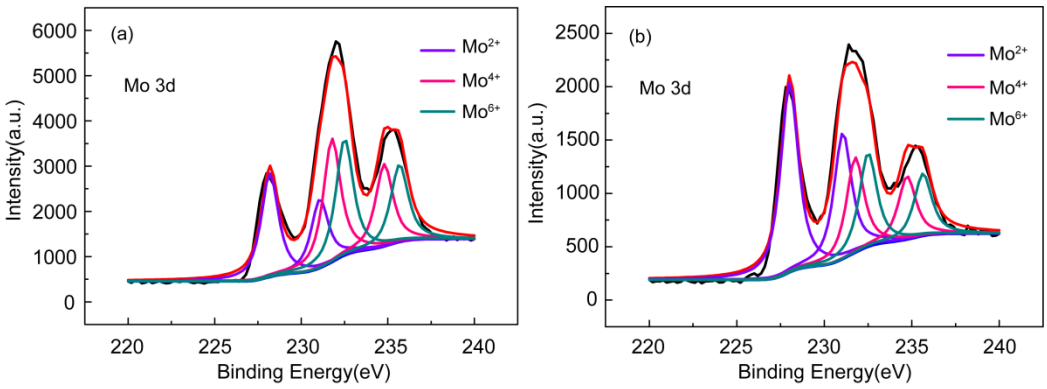

Fig. 3 XPS Mo 3*d* spectra of Mo_2C/SS (a) and Mo_2C (b).

Table 1 The peak position and percentage of Mo at different valence states in Mo_2C/SS and Mo_2C.

	Species	Peak position/eV	Percentage/%
Mo_2C/SS	Mo^{2+}	228.18; 231.07	30.13
	Mo^{4+}	231.7; 234.79	35.90
	Mo^{6+}	232.50; 235.67	33.97
Mo_2C	Mo^{2+}	228.01; 231.05	50.08
	Mo^{4+}	231.76; 234.73	25.13
	Mo^{6+}	232.50; 235.63	24.79

catalytic activity and nearly zero onset overpotential. Compared with the Mo_2C, Mo_2C/SS exhibits an obvious better HER performance with an overpotential of 175 mV to drive a current density of 10 mA·cm^{-2}, which is the approximate current density expected for a 10% efficient solar-to-fuels conversion device under 1 sun illumination [23]. The HER activity of molybdenum oxides can be neglected compared with molybdenum carbides, which can be shown in Supporting Information Fig. S2. And the summary of the previously reported molybdenum carbides in acidic media was placed in Supporting Information Table S1.

The Tafel slope is obtained by fitting the Tafel equation $\eta = b\lg j + a$, where j is the current density and b is the Tafel slope. A smaller Tafel slope means a faster HER rate with the increasing overpotential and so it can serve as one of the most intuitive measure of HER activity [24] . As shown in Fig. 4b, the Tafel slope of Mo_2C (145 mV·dec^{-1}) is much larger than that of Mo_2C/SS (88 mV·dec^{-1}). The nanoparticles in Mo_2C have a larger size with serious aggregation, the transport of protons or electrons might be limited in specific regions, which influences HER performance and corresponding Tafel slope [18,25].

In addition, the Tafel slope can also be used to initially infer the possible HER mechanism on the catalyst since the Tafel slope is an inherent property of the catalyst determined by the rate-determining step of HER. In general, three principal steps may be involved in acidic solution during the process of HER [18,26].

Discharge step: $H^+ + e^- \rightarrow H_{ads}$ (Volmer reaction)

Recombination step: $H_{ads} + H_{ads} \rightarrow H_2$ (Tafel reaction)

Electrochemical desorption step: $H_{ads} + H^+ + e^- \rightarrow H_2$ (Heyrovsky reaction)

The proton is initially adsorbed on the surface of the catalyst *via* the discharge step, known as Volmer step, followed by a chemical desorption step (Tafel step) or an electrochemical desorption step (Heyrovsky step) to remove the hydrogen molecules. According to previous reports, a Tafel slope of 120 mV·dec^{-1} is indicative of a reaction whose rate is limited by the Volmer step, while 30 and 40 mV·dec^{-1} will be obtained for reaction limited by Tafel step and Heyrovsky step respectively. As shown in Fig. 3b, the Tafel slope for commercial Pt/C is 30 mV·dec^{-1}, which is consistent with previous reports and the HER process on commercial Pt/C should follow Volmer-Tafel mechanism with the Tafel step as the rate-limiting step [27]. The Tafel slope of Mo_2C/SS (88 mV·dec^{-1}) falls within the range of

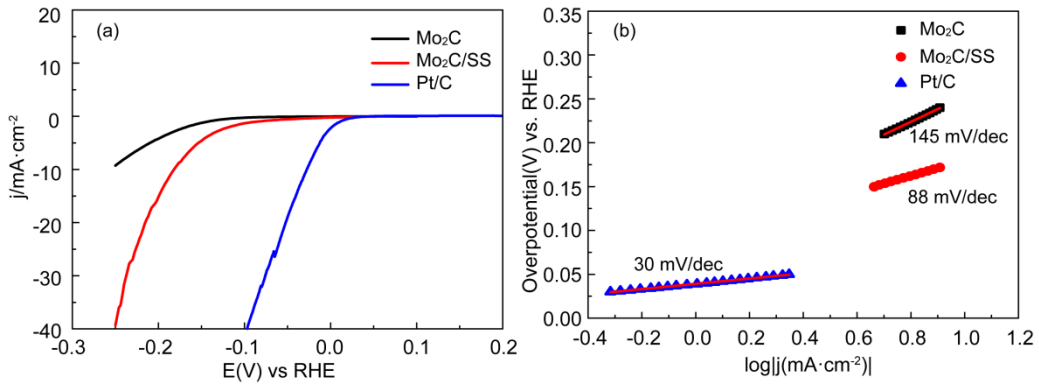

Fig. 4 (a) Polarization curves and (b) the corresponding Tafel plots of Mo_2C/SS, Mo_2C and commercial Pt/C.

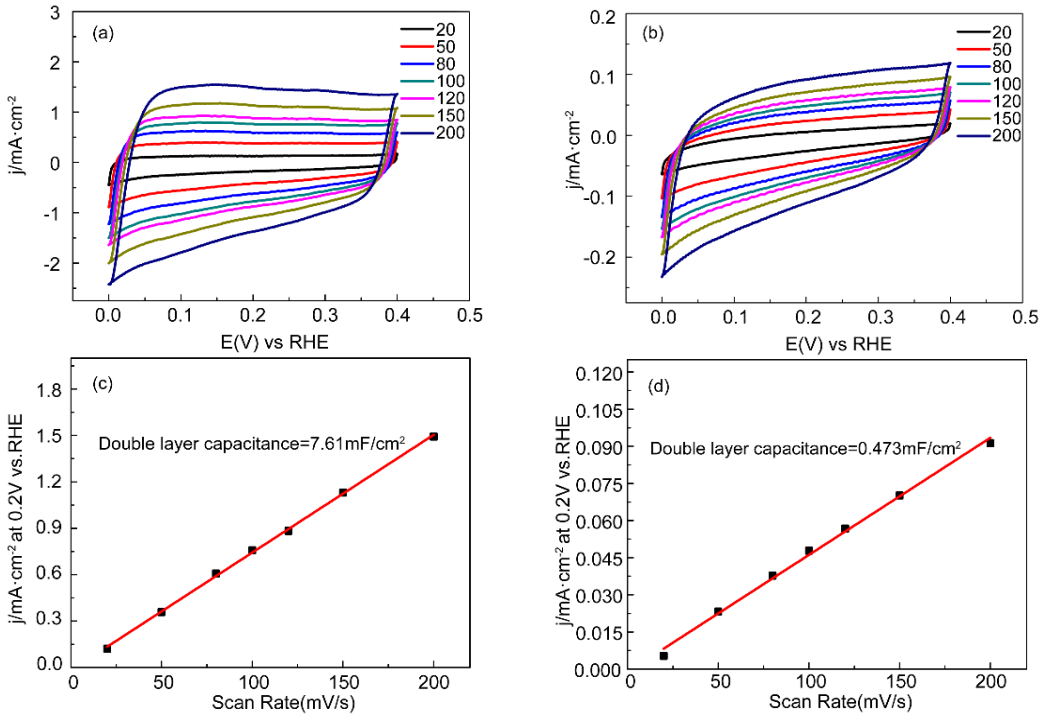

Fig. 5 CV curves of Mo_2C/SS (a) and Mo_2C (b) at different scan rates from 20 to 200 mV·s^{-1}; capacitive current at 0.2 V as a function of scan rates for Mo_2C/SS (c) and Mo_2C (d).

40–120 mV·dec^{-1}, suggesting that hydrogen production on the catalyst proceeds through Volmer-Heyrovsky mechanism where the electrochemical desorption is the rate-determining step [18,28]. The value of Tafel slope for Mo_2C (145 mV·dec^{-1}), near the ideal value for the Volmer step (120 mV·dec^{-1}), which indicates that the proton adsorption on the catalyst is relatively difficult revealing that the Volmer step is the rate determining step for HER. The lower Tafel slope at Mo_2C/SS than Mo_2C also indicated the higher efficiency of water dissociation.

Fig. 5a, b show the CV curves of Mo_2C/SS and Mo_2C at scan rates ranging from 20 to 200 mV·s^{-1}, fitting the capacitive current at 0.2 V as a linear function of scan rates and the slope is the double layer capacitance. Therefore the obtained double layer capacitances of Mo_2C/SS and Mo_2C are 7.61 and 0.473 mF·cm^{-2}, respectively.

Electrochemical surface area (ECSA) is the ratio of the double layer capacitance to the specific capacitance for a flat surface, so the value of ECSA can be calculated as follows [29,30]:

$$\mathrm{ECSA} = \frac{\text{double layer capacitance}}{\text{specific capacitance}}$$

The specific capacitance for a flat surface is usually found to fall within the range of 20–60 μF·cm^{-2}. Because for many metals and semiconductors, the double layer capacitance after surface area normalization is comparable in the same electrolyte, therefore the moderate value of 40 μF·cm^{-2} is adopted in this paper for the following calculations [31,32].

The number of active sites per surface area was calculated according to the crystal data as follows [29]:

$$= \left(\frac{2\ \text{atoms}\cdot\text{unit cell}^{-1}}{37.2\ \text{Å}^3\cdot\text{unit cell}^{-1}}\right)^{\frac{2}{3}}$$

$$= 1.42\times10^{15}\ \text{atoms}\cdot\text{cm}^{-2}$$

For Mo_2C/SS, the double layer capacitance is 7.61 mF·cm^{-2}

$$\mathrm{ECSA} = \frac{7.61\ \text{mF}\cdot\text{cm}^{-2}}{40\ \mu\text{F}\cdot\text{cm}^{-2}\ \text{per cm}^2}$$

$$= 190.25\ \text{cm}^2$$

The number of surface active sites = 1.42 × 10^{15} atoms·cm^{-2} × 190.25 cm^2 = 2.70× 10^{17}

For Mo_2C, we can also calculate as following:

$$\mathrm{ECSA} = \frac{0.473\ \text{mF}\cdot\text{cm}^{-2}}{40\ \mu\text{F}\cdot\text{cm}^{-2}\ \text{per cm}^2}$$

$$= 11.83\ \text{cm}^2$$

The number of surface active sites = 1.42 × 10^{15} atoms·cm^{-2} × 11.83 cm^2 =1.68× 10^{16}

The number of total hydrogen turnovers was calculated from the current density according to the formula [33]:

$$= \left(j\frac{\text{mA}}{\text{cm}^2}\right)\left(\frac{1\ \text{C}\cdot\text{s}^{-1}}{1000\ \text{mA}}\right)\left(\frac{1\ \text{mol e}^-}{96485\ \text{C}}\right)\left(\frac{1\ \text{mol H}_2}{2\ \text{mol e}^-}\right)\left(\frac{6.02\times10^{23}\ \text{H}_2}{1\ \text{mol H}_2}\right)$$

$$= 3.12\times10^{15}\frac{\text{H}_2\cdot\text{s}^{-1}}{\text{cm}^2}\ \text{per}\ \frac{\text{mA}}{\text{cm}^2}$$

Turnover frequency (TOF) refers to the rate of hydrogen production per active site, the number of TOF can be calculated as the following formula [29]:

$$\mathrm{TOF} = \frac{3.12\times10^{15}\times|j|}{\text{The number of surface active sites}}$$

where j is the current density at the overpotential of 200 mV, which can be obtained from HER polarization curves (shown in Fig. 4). Therefore the acquired j for Mo_2C/SS and Mo_2C are

15.96 and 4.52 mA·cm^{-2}, respectively.

Therefore we can calculate the TOF numbers for Mo_2C/SS and Mo_2C as follows:

For Mo_2C/SS:

$$\mathrm{TOF}_{(\mathrm{at}\,\eta=200\ \mathrm{mv})} = \frac{3.12\times10^{15}\times15.96}{2.70\times10^{17}} = 0.185\frac{\mathrm{H_2\cdot s^{-1}}}{\mathrm{surface\ site}}$$

and for Mo_2C:

$$\mathrm{TOF}_{(\mathrm{at}\,\eta=200\ \mathrm{mv})} = \frac{3.12\times10^{15}\times4.52}{1.68\times10^{16}} = 0.840\frac{\mathrm{H_2\cdot s^{-1}}}{\mathrm{surface\ site}}$$

Compare the number of surface active sites and TOF of the product, it can be found that the number of surface active sites can increase for more than 15 times *via* salt sealing, which indicates that the generation of pores is beneficial to exposing more active sites. While the TOF number decreases after salt sealing, which can be analyzed with the results of XPS and the value of ECSA. At the potential of 0.2 V, no faradic processes of HER are observed, while the faradic reaction of molybdenum oxides on the catalyst surface are present during the process of double layer charging and discharging, which leads to the existence of pseudocapacitance. According to previous reports [34,35], the pseudocapacitance materials exhibit the property of capacitance due to redox reaction occured on them. As one kind of pseudocapacitance materials, metal oxides have specific capacitances 10–100 times higher than that of double layer materials and have drawn increasing attention in recent years. As a typical pseudocapacitance material, RuO_2 has been prepared in various methods in recent years [36,37]. For instance, Hu *et al.* [38] synthesized RuO_2 nanotubes with a high specific capacitance of 1300 F·g^{-1}, which can be used as a good material for supercapacitors. While the high cost of RuO_2 limits its commercial applications. NiO has been regarded as a promising substitute for RuO_2 as a pseudocapacitance material due to its relatively lower price and has been applied in alkaline supercapacitor systems [39]. In addition to RuO_2, NiO, the pseudocapacitance phenomenon of other transition metal oxides such as CoO and MoO_2 has also been widely studied [40,41]. The pseudocapacitance generated by molybdenum oxides will be superimposed with the double layer capacitance of Mo_2C catalysts, which increases the specific capacity. In other words, the obtained double layer capacitances in our manuscript include not only the bilayer capacitance of molybdenum carbides but also involve the contribution of pseudocapacitance from the faradic reaction of molybdenum oxides, which leads to the enlarged double layer capacitances. Taking into account the results of XPS, the percentage of molybdenum oxides on Mo_2C/SS (69.87%) is obviously higher than that of Mo_2C (49.92%), that is to say the effect of pseudocapacitance on Mo_2C/SS is more significant. On the other hand, j obtained from HER polarization curves mainly derives from active centers (molybdenum carbides) of HER, while with the form of pores by salt sealing, the contact area with oxygen increases, so higher content of molybdenum oxides is generated on the surface, resulting in a lower proportion of molybdenum carbides on the surface of catalyst, therefore the TOF number declines after salt sealing.

The stability is another important indicator of the catalytic performance of a HER catalyst. The stability test of Mo_2C/SS and Mo_2C were placed in Supporting Information Fig. S3.

4 Conclusions

In summary, Mo_2C/SS was successfully synthesized as an electrocatalyst for enhanced hydrogen evolution and the Mo_2C without salt sealing was prepared for comparison. Compared with Mo_2C, Mo_2C/SS holds three favorable features for a better HER mass activity: (1) The generation of large quantities of pores *via* salt sealing contributes to increase the BET surface area and expose more active sites, which is beneficial for improving HER performance; (2) The porous structure and enlarged surface area pave the way for effective mass and charge transfer; (3) The Tafel slope decreased from 145 to 88 mV·dec^{-1}. For the first time, the strategy of salt sealing was applied for creating pores in molybdenum carbide, which had been proved to be an efficient electrocatalyst for enhanced hydrogen evolution.

Supporting Information: available free of charge *via* the internet at http://www.whxb.pku.edu.cn.

References

(1) Xing, Z. C.; Liu, Q.; Asiri, A. M.; Sun, X. P. *ACS Catal.* **2015,** *5*, 145. doi: 10.1021/cs5014943

(2) Michalsky, R.; Zhang, Y. J.; Peterson, A. A. *ACS Catal.* **2014,** *4*, 1274. doi: 10.1021/cs500056u

(3) Tang, Q.; Jiang, D. E. *ACS Catal.* **2016,** *6,* 4953. doi: 10.1021/acscatal.6b01211

(4) Zheng, Y.; Jiao, Y.; Jaroniec, M.; Qiao, S. Z. *Angew. Chem. Int. Edit.* **2015,** *54*, 52. doi: 10.1002/anie.201407031

(5) Wang, J. J.; Wang, W.; Wang, Z. Y.; Chen, J. G. G.; Liu, C. J. *ACS Catal.* **2016,** *6*, 6585. doi: 10.1021/acscatal.6b01927

(6) Lu, Q.; Hutchings, G. S.; Yu, W. T.; Zhou, Y.; Forest, R. V.; Tao, R. Z.; Rosen, J.; Yonemoto, B. T.; Cao, Z. Y.; Zheng, H. M.; *et al. Nat. Commun.* **2015,** *6*, 6567. doi: 10.1038/ncomms7567

(7) Kelly, T. G.; Chen, J. G. *Chem. Soc. Rev.* **2012,** *41*, 8021. doi: 10.1039/c2cs35165j

(8) Chang, J. F.; Xiao, Y.; Luo, Z. Y.; Ge, J. J.; Liu, C. P.; Xing, W. *Acta Phys. -Chim. Sin.* **2016,** *32*, 1556. [常进法, 肖瑶, 罗兆艳, 葛君杰, 刘长鹏, 邢巍. 物理化学学报, **2016,** *32*, 1556.] doi: 10.3866/PKU.WHXB201604291

(9) Sheng, J. F.; Ma, C. A.; Zhang, C.; Li, G. H. *Acta Phys. -Chim. Sin.* **2007,** *23*, 181. [盛江峰, 马淳安, 张诚, 李国华. 物理化学学报, **2007,** *23*, 181.] doi: 10.3866/PKU.WHXB20070209

(10) Cao, P. F.; Hu, Y.; Zhang, Y. W.; Peng, J.; Zhai, M. L. *Acta Phys. -Chim. Sin.* **2017,** *33*, 2542. [曹朋飞, 胡杨, 张有为, 彭静, 翟茂林. 物理化学学报, **2017,** *33*, 2542.] doi: 10.3866/PKU.WHXB201706151

(11) Wu, Y.; Luo, J. *Acta Phys. -Chim. Sin.* **2016,** *32*, 2745. [吴昱, 罗键. 物理化学学报, **2016,** *32*, 2745.] doi: 10.3866/PKU.WHXB201608083

(12) Cao, Y. L.; Wang, F.; Liu, J. J.; Wang, J. J. Zhang, L. H.; Qin, S. Y. *Acta Phys. -Chim. Sin.* **2009,** *25*, 1979. [曹寅亮, 王峰, 刘景军, 王建军, 张良虎, 覃事永. 物理化学学报, **2009,** *25*, 1979.] doi: 10.3866/PKU.WHXB20091017

(13) Duan, J. J.; Chen, S.; Chambers, B. A.; Andersson, G. G.; Qiao, S. Z. *Adv. Mater.* **2015,** *27*, 4234. doi: 10.1002/adma.201501692

(14) Lu, Q. P.; Yu, Y. F.; Ma, Q. L.; Chen, B.; Zhang, H. *Adv. Mater.* **2016,** *28*, 1917. doi: 10.1002/adma.201503270

(15) Wan, C.; Regmi, Y. N.; Leonard, B. M. *Angew. Chem. Int. Edit.* **2014,** *53*, 6407. doi: 10.1002/anie.201402998

(16) Ang, H. X.; Tan, H. T.; Luo, Z. M.; Zhang, Y.; Guo, Y. Y.; Guo, G. L.; Zhang, H.; Yan, Q. Y. *Small* **2015,** *11*, 6278. doi: 10.1002/smll.201502106

(17) Cui, W.; Cheng, N. Y.; Liu, Q.; Ge, C. J.; Asiri, A. M.; Sun, X. P. *ACS Catal.* **2014,** *4*, 2658. doi: 10.1021/cs5005294

(18) Liao, L.; Wang, S. N.; Xiao, J. J.; Bian, X. J.; Zhang, Y. H.; Scanlon, M. D.; Hu, X. L.; Tang, Y.; Liu, B. H.; Girault, H. H. *Energy Environ. Sci.* **2014,** *7*, 387. doi: 10.1039/c3ee42441c

(19) Ding, W.; Li, L.; Xiong, K.; Wang, Y.; Li, W.; Nie, Y.; Chen, S. G.; Qi, X. Q.; Wei, Z. D. *J. Am. Chem. Soc.* **2015,** *137*, 5414. doi: 10.1021/jacs.5b00292

(20) Chen, W. F.; Sasaki, K.; Ma, C.; Frenkel, A. I.; Marinkovic, N.; Muckerman, J. T.; Zhu, Y. M.; Adzic, R. R. *Angew. Chem. Int. Edit.* **2012,** *51*, 6131. doi: 10.1002/anie.201200699

(21) Xiao, P.; Yan, Y.; Ge, X. M.; Liu, Z. L.; Wang, J. Y.; Wang, X. *Appl. Catal. B-Environ.* **2014,** *154*, 232. doi: 10.1016/j.apcatb.2014.02.020

(22) Park, H.; Encinas, A.; Scheifers, J. P.; Zhang, Y.; Fokwa, B. P. T. *Angew. Chem. Int. Edit.* **2017,** *56*, 5575. doi:10.1002/anie.201611756

(23) McCrory, C. C. L.; Jung, S.; Ferrer, I. M.; Chatman, S. M.; Peters, J. C.; Jaramillo, T. F. *J. Am. Chem. Soc.* **2015,** *137*, 4347. doi: 10.1021/ja510442p

(24) Merki, D.; Hu, X. L. *Energy Environ. Sci.* **2011,** *4*, 3878. doi: 10.1039/c1ee01970h

(25) Vrubel, H.; Hu, X. L. *Angew. Chem. Int. Edit.* **2012,** *51*, 12703. doi: 10.1002/anie.201207111

(26) Conway, B. E.; Tilak, B. V. *Electrochim. Acta* **2002,** *47*, 3571. doi: 10.1016/S0013-4686(02)00329-8

(27) Li, Y.; Wang, H.; Xie, L.; Liang, Y.; Hong, G.; Dai, H. *J. Am. Chem. Soc.* **2011,** *133*, 7296. doi: 10.1021/ja201269b

(28) Li, Y.; Li, H.; Cao, K.; Jin, T.; Wang, X.; Sun, H.; Ning, J.; Wang, Y. Jiao, L. *Energy Storage Mater.* **2018,** *12*, 44. doi: 10.1016/j.ensm.2017.11.006

(29) Tang, C.; Wang, W.; Sun, A.; Qi, C.; Zhang, D.; Wu, Z.; Wang, D. *ACS Catal.* **2015,** *5*, 6956. doi: 10.1021/acscatal.5b01803

(30) Ye, R. Q.; del Angel-Vicente, P.; Liu, Y. Y.; Arellano-Jimenez, M. J.; Peng, Z. W.; Wang, T.; Li, Y. L.; Yakobson, B. I.; Wei, S. H.; Yacaman, M. J.; *et al*. *Adv. Mater.* **2016,** *28*, 1427. doi: 10.1002/adma.201504866

(31) Kibsgaard, J.; Jaramillo, T. F. *Angew. Chem. Int. Edit.* **2014,** *53*, 14433. doi: 10.1002/anie.201408222

(32) Kucernak, A. R. J.; Sundaram, V. N. N. *J. Mater. Chem. A* **2014,** *2*, 17435. doi: 10.1039/c4ta03468f

(33) Chen, Y. Y.; Zhang, Y.; Jiang, W. J.; Zhang, X.; Dai, Z. H.; Wan, L. J.; Hu, J. S. *ACS Nano* **2016,** *10*, 8851. doi: 10.1021/acsnano.6b04725

(34) Brezesinski, T.; Wang, J.; Tolbert, S. H.; Dunn, B. *Nat. Mater.* **2010,** *9*, 146. doi: 10.1038/nmat2612

(35) Lang, X.; Hirata, A.; Fujita, T.; Chen, M. *Nat. Nanotechnol.* **2011,** *6*, 232. doi: 10.1038/nnano.2011.13

(36) Sugimoto, W.; Iwata, H.; Yokoshima, K.; Murakami, Y.; Takasu, Y. *J. Phys. Chem. B* **2005,** *109*, 7330. doi: 10.1021/jp044252o

(37) Hu, C. C.; Chen, W. C. *Electrochim. Acta* .**2004,** *49*, 3469. doi: 10.1016/j.electacta.2004.03.017

(38) Hu, C. C.; Chang, K .H.; Lin, M. C.; Wu, Y. T. *Nano Lett*. **2006,** *6*, 2690. doi: 10.1021/nl061576a

(39) Zhang, Y.; Zhou, Z.; Yan, J. *J. Power Sources* **1998,** *75*, 283. doi: 10.1016/S0378-7753(98)00111-6

(40) Cao, F.; Pan, G. X.; Tang, P. S;. Chen, H. F. *J. Power Sources* **2012,** *216*, 395. doi: 10.1016/j.jpowsour.2012.05.073

(41) Rajeswari, J.; Kishore, P. S.; Viswanathan, B.; Varadarajan, T. K. *Electrochem. Commun.* **2009,** *11*, 572. doi: 10.1016/j.elecom.2008.12.050